

Structured Jet Model for Multiwavelength Observations of the Jetted Tidal Disruption Event AT 2022cmc

CHENGCHAO YUAN (袁成超),¹ B. THEODORE ZHANG (张兵),² WALTER WINTER,¹ AND KOHTA MURASE^{3,2}

¹*Deutsches Elektronen-Synchrotron DESY, Platanenallee 6, 15738 Zeuthen, Germany*

²*Center for Gravitational Physics and Quantum Information, Yukawa Institute for Theoretical Physics, Kyoto University, Kyoto, Kyoto 606-8502, Japan*

³*Department of Physics, Department of Astronomy & Astrophysics, Center for Multimessenger Astrophysics, Institute for Gravitation and the Cosmos, The Pennsylvania State University, University Park, PA 16802, USA*

ABSTRACT

AT 2022cmc is a recently documented tidal disruption event (TDE) that exhibits a luminous jet, accompanied by fast-declining X-ray and long-lasting radio/millimeter emission. Motivated by the distinct spectral and temporal signatures between X-ray and radio observations, we propose a multizone model involving relativistic jets with different Lorentz factors. We systematically study the evolution of the faster and slower jets in an external density profile, considering the continuous energy injection rate associated with the time-dependent accretion rates before and after the mass fallback time. We investigate time-dependent multiwavelength emission from both the forward shock and reverse shock regions of the fast and slow jets, in a self-consistent manner. Our analysis demonstrates that the energy injection rate can significantly impact the jet evolution and subsequently influence the lightcurves. We find that the X-ray spectra and lightcurves can be described by the electron synchrotron emission from the reverse shock of the faster jet, in which the late-time X-ray upper limits, extending to 400 days after the disruption, could be interpreted as the jet break. Meanwhile, the radio observations can be interpreted as a result of synchrotron emission from the forward shock region of the slower jet. We also discuss prospects for testing the model with current and future observations.

Keywords: Tidal disruption events; relativistic jets; transient; radiative processes

1. INTRODUCTION

Tidal disruption events (TDEs) are astronomical phenomena that occur when a star is torn apart by the gravitational forces of a supermassive black hole as the star orbits in close proximity to the supermassive black hole (SMBH, e.g., Hills 1975; Rees 1988; Evans & Kochanek 1989). The subsequent accretion activities, fueled by the bound mass of the star, can generate a luminous transient spanning a broad electromagnetic spectrum, including radio, optical, ultraviolet, X-ray, and γ -ray bands. Among the expanding catalog of recorded TDEs, four TDEs, including Swift J1644+57 (Bloom et al. 2011; Burrows et al. 2011), Swift J2058+05 (Cenko et al. 2012), Swift J1112-8238 (Brown et al. 2015) and AT 2022cmc (Andreoni et al. 2022), have been classified as jetted TDEs. These jetted TDEs display promi-

nent signatures of relativistic outflows, including fast-decaying lightcurves and nonthermal flux intensities in X-ray bands, alongside bright, long-lived radio emission (e.g., Pasham et al. 2023; Yao et al. 2024).

It has been thought that the radio emission is explained by synchrotron emission of electrons accelerated at external forward shocks (e.g., Zauderer et al. 2011; Giannios & Metzger 2011; Metzger et al. 2012; Berger et al. 2012; Zauderer et al. 2013; Eftekhari et al. 2018; Cendes et al. 2021; Matsumoto & Metzger 2023) as the jet propagates into the circumnuclear medium and becomes decelerated, resembling the physics of gamma-ray burst (GRB) afterglows (e.g., Zhang 2018).

As for X-ray emission from jetted TDEs, interpreting them within the same emission zone for the radio emission is challenging. Different sites or mechanisms — such as the magnetically dominated jet (Burrows et al. 2011), variable accretion near the SMBH horizon (Reis et al. 2012), inverse Compton scattering of external photons (Bloom et al. 2011; Crumley et al. 2016) — are

proposed to describe the X-ray observations. A self-consistent physical framework is needed to interpret the multiwavelength spectral energy distributions (SEDs) and the temporal evolutions of radio and X-ray emission.

The recent documented jetted TDE AT 2022cmc at redshift $z = 1.19$ provides us another prototype for multiwavelength modeling. AT 2022cmc was discovered by the Zwicky Transient Facility (ZTF) in the optical band (Andreoni et al. 2022). The short variability time scale in the SMBH rest frame, $t_{\text{var}} \lesssim 1000 \text{ s}/(1+z)$, implies an upper limit of the SMBH mass of few $\times 10^7 M_{\odot}$ (Yao et al. 2024). A relativistic jet with high Lorentz factor ~ 100 was initially suggested to explain its super luminous and fast evolving X-ray (e.g., $L_X \propto t^{-2}$) and long-lasting radio emissions (Pasham et al. 2023). Moreover, an equipartition analysis (e.g., Chevalier 1998; Barniol Duran et al. 2013) and a detailed afterglow model reveals the radio/millimeter emitting plasma to be expanding relativistically (Matsumoto & Metzger 2023; Yao et al. 2024), e.g., $\Gamma \lesssim 2 - 5$. The two-component jet model with a fast inner component and slow outer component, and has also been exploited to explain the multiwavelength emission from TDEs (Wang et al. 2014; Mimica et al. 2015; Liu et al. 2015; Teboul & Metzger 2023; Sato et al. 2024). Recently, Zhou et al. (2024) demonstrated that the early and late radio emission of AT 2022cmc can be described by the forward shocks of fast and slow jets but in the best-fitting cases the model is insufficient to reproduce X-ray lightcurves, which implies that the radio/millimeter and X-ray may have different origins.

Motivated by the distinct signatures between radio/millimeter and X-ray signals, such as their lightcurves (e.g., long-lasting vs. fast-decaying), their variability time scales (e.g., day-time-scale (Rhodes et al. 2023) vs. $\sim 10^3 \text{ s}$), and their spectral shapes (e.g., synchrotron self-absorption tail vs. synchrotron broken power-law), we present a multizone model incorporating a fast relativistic jet (narrow outflow, denoted as ‘fast jet’) and a slow relativistic jet (wide outflow, denoted as ‘slow jet’) capable of explaining the X-ray and radio SEDs and lightcurves simultaneously. In addition to TDEs, structured jets have been extensively studied in the context of GRBs for a long time (e.g., Rossi et al. 2002; Zhang & Mészáros 2002; Sato et al. 2021; Zhang et al. 2023).

In this work, following the treatment for GRB blast waves (Nava et al. 2013; Zhang 2018; Zhang et al. 2023), we solve the differential equations governing the time evolution of jets sweeping an external medium, taking into account the time-dependent continuous energy/mass injections. We then compute the time-

dependent synchrotron and inverse Compton emission from the forward shock and reverse shock regions. Our results demonstrate that the radio/millimeter observations can be explained by the forward shock model of the slow jet, and the fast jet reverse shock synchrotron emissions can reproduce the X-ray spectra and lightcurve. We also argue that the steepening of the late-time (approximately 200–400 days after disruption) X-ray lightcurve, as reported in Eftekhari et al. (2024), could be attributed to the jet break as the jet Lorentz factor decreases.

The paper is organized as follows. In Sec. 2, we model the accretion history. The physical picture and time evolution of jets are presented in Sec. 3. We then apply the dynamics of jets to compute the time-dependent synchrotron and inverse Compton emissions in the jet forward shock and reverse shock regions of the fast and slow jets in Sec. 4, where the radio/millimeter and X-ray SEDs in three epochs (15-16 d, 25-27 d and 41-46 d in the observer’s frame) and lightcurves extending to 400 days after the disruption are also fitted. A discussion and a summary are given in Sec. 5 and Sec. 6, respectively.

Throughout the paper, we use T , t , and t' to denote the times measured in the observer’s frame, SMBH-rest frame, and jet comoving frame, respectively. The subscripts ‘f’ and ‘s’ will be used to denote the quantities related to fast and slow jets. The notation Q_x represents $Q/10^x$ in CGS units unless otherwise specified.

2. ACCRETION RATE ONTO THE SMBH

Considering the disruption of a star of mass M_{\star} and radius R_{\star} by a SMBH of mass M_{BH} , we estimate the tidal radius to be $R_T \approx f_T (M_{\text{BH}}/M_{\star})^{1/3} R_{\star}$ (e.g., Rees 1988), where $f_T \sim 0.02$ to 0.3 , accounting for corrections from the stellar internal density profile (e.g., Phinney 1989; Piran et al. 2015). For a main sequence star, the radius can be related to the mass via $R_{\star} = R_{\odot} (M_{\star}/M_{\odot})^{1-\xi}$, where R_{\odot} and M_{\odot} are the solar radius and mass respectively, and the parameter $\xi \sim 0.4$ for $1 < M_{\star}/M_{\odot} < 10$ (Kippenhahn & Weigert 1990). Based on the rather loose constraints on the SMBH mass of AT 2022cmc, e.g., $M_{\text{BH}} < 5 \times 10^8 M_{\odot}$ (Andreoni et al. 2022), and the upper limit obtained from the X-ray variability, e.g., $M_{\text{BH}} < 5 \times 10^7 M_{\odot}$ (Yao et al. 2024), we select $M_{\text{BH}} = 10^7 M_{\text{BH},7} M_{\odot}$ and $M_{\star} = 5 M_{\star,0.7} M_{\odot}$ as the fiducial parameters¹ and obtain the corresponding tidal radius $R_T \simeq 1.2 \times 10^{13} \text{ cm}$. After undergoing tidal disruption, approximately half of the stellar

¹ The value of M_{\star} is degenerate with the energy conversion efficiencies and will be justified in Sec. 5

material may persist in a gravitationally bound state within an eccentric orbit, ultimately leading to its return and potential accretion onto the SMBH. The fallback time can be estimated using the orbital period of the most tightly bound matter, expressed explicitly as $t_{\text{fb}} \approx 2\pi\sqrt{a_{\text{min}}^3/GM_{\text{BH}}}$, where $a_{\text{min}} \approx R_T^2/(2R_*)$ is the semi-major axis of the orbit. In our fiducial case, we have $t_{\text{fb}} \simeq 3.3 \times 10^6 \text{ s } f_{T,-1.2}^{1/2} M_{\text{BH},7}^{1/2} M_{*,0.7}^{-1/10}$.

The mass fallback could result in the formation of an accretion disk, with the accretion rate onto the SMBH following a $t^{-5/3}$ proportionality law after the fallback time. Here, t denotes the time measured in the rest frame of the SMBH, which can be correlated with the observation time, T_{obs} , through $t = T_{\text{obs}}/(1+z)$. Accretion may also occur prior to t_{fb} . For instance, Metzger et al. (2012) investigated a constant early-stage accretion rate to explain the radio emission from the jetted TDE Swift J1644+57. In this study, for generality, we presume a power-law decay in the accretion rate before the fallback of the most tightly bound material and explicitly express the time-dependent accretion rates before and after t_{fb} as

$$\dot{M}_{\text{BH}} = \frac{\eta_{\text{acc}} M_*}{\mathcal{C} t_{\text{fb}}} \times \begin{cases} \left(\frac{t}{t_{\text{fb}}}\right)^{-\alpha}, & t < t_{\text{fb}} \\ \left(\frac{t}{t_{\text{fb}}}\right)^{-5/3}, & t > t_{\text{fb}}, \end{cases} \quad (1)$$

where $0 \leq \alpha < 1$ is the free early-time accretion index², the accretion efficiency η_{acc} represents the fraction of bounded materials that eventually ends up being accreted to the SMBH, and $\mathcal{C} \equiv 3 + 2/(1 - \alpha)$ is introduced to normalize the total accreted mass, e.g., $\int \dot{M}_{\text{BH}} dt = \eta_{\text{acc}} M_*/2$. The accretion efficiency, η_{acc} , typically depends on the dynamics of mass fallback and disk formation, since typically a fraction of mass would fallback and end up forming a disk. Nevertheless, for simplicity, we opt for a constant value of $\eta_{\text{acc}} = 0.1$ (Murase et al. 2020), noting its degeneracy with other parameters. Hence, the accretion rate at t_{fb} can be explicitly written as

$$\begin{aligned} \dot{M}_{\text{BH}}(t_{\text{fb}}) c^2 &\simeq 5.5 \times 10^{46} \text{ erg s}^{-1} \eta_{\text{acc},-1} \mathcal{C}_{0.7} \\ &\times f_{T,-1.2}^{-1/2} M_{\text{BH},7}^{-1/2} M_{*,0.7}^{1.1}, \end{aligned} \quad (2)$$

which implies the accretion rate is initially in the super-Eddington regime, e.g., $\dot{M}_{\text{BH}} c^2 \gtrsim L_{\text{Edd}}/\eta_{\text{rad}} \simeq 1.26 \times 10^{46} M_{\text{BH},7} \eta_{\text{rad},-1}^{-1} \text{ erg s}^{-1}$, where L_{Edd} is the Eddington luminosity and $\eta_{\text{rad}} \sim 0.1$ is the radiation efficiency.

² Shen & Matzner (2014) pointed out that a slow-decaying accretion rate is possible due to disk internal kinematic viscosity, depending on the type of polytrope stars.

3. JET DYNAMICS

In this section, we describe the physical framework of our structured jet model and derive the time evolution of jet Lorentz factors incorporating the continuous energy and mass injections. These derivations will be used in Sec. 4 to compute the time-dependent electromagnetic emissions.

3.1. The physical picture

Multiwavelength follow-ups of AT 2022cmc demonstrate distinct signatures between radio, optical and X-ray emissions, which imply that they may originate from different radiation zones.

Firstly, regarding the spectral energy distributions (SEDs), we find that the radio spectra align with synchrotron self-absorption tails in the electron slow-cooling regime. The optical spectra exhibit good agreement with black body distributions whereas the X-ray spectra are consistent with either a single power-law or a broken power-law distribution predicted by synchrotron radiation (Pasham et al. 2023; Yao et al. 2024). In this case, these emissions likely stem from different physical environments characterized by distinct compactness and magnetic fields. For example, the radio and X-ray emissions may be generated by nonthermal electrons accelerated in extended shocks, while the thermal optical emissions probably originate from a thermal envelope within the accretion disk or a hot corona.

Secondly, concerning the temporal evolution, the radio signals display a long-lasting lightcurve, contrasting with the rapidly decaying X-ray lightcurves, which implies that these emissions might be produced in different regions governed by disparate kinetic equations and initial conditions. A relativistic jet with a Lorentz factor greater than 10 is favored to explain the bright and hard X-ray emissions. Zhou et al. (2024) also demonstrated that a single wide/slow jet similar to GRB afterglow models is insufficient to reproduce the radio and X-ray observations simultaneously.

Motivated by these considerations, we propose a time-dependent structured jet model, where the fast/narrow jet and the slow/wide jet are respectively adopted to explain the X-ray and radio lightcurves and spectra at various epochs. Fig. 1 illustrates the configuration of our multizone model, depicting an accretion disk, a fast jet with Lorentz factor Γ_f , and a slow jet with Lorentz factor Γ_s . As for the density profile of the external medium, we connect a circumnuclear envelope within the radius R_{env} to the interstellar medium. We explicitly write down the density profile (in the units of cm^{-3}) in terms

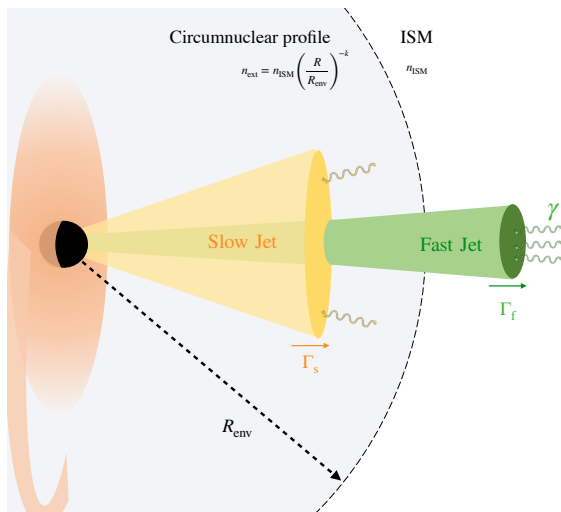


Figure 1. The schematic picture of the structured jet model. A slow jet propagating with Lorentz factor Γ_s in the circumnuclear envelope ($R_s < R_{\text{env}}$) and a fast jet with Lorentz factor Γ_f propagating in an ISM ($R_f > R_{\text{env}}$) are illustrated.

of the distance (R) to the SMBH,

$$n_{\text{ext}}(R) = \begin{cases} n_{\text{ISM}} \left(\frac{R}{R_{\text{env}}}\right)^{-k}, & R < R_{\text{env}} \\ n_{\text{ISM}}, & R > R_{\text{env}} \end{cases} \quad (3)$$

where n_{ISM} is the number density of ISM, $1.5 \leq k \leq 2$ is index of the density profile within the envelope radius R_{env} as suggested by the radio data fitting (e.g., Matsumoto & Metzger 2023; Yao et al. 2024; Zhou et al. 2024). One potential source of the circumnuclear envelope is the wind emanating from pre-existing disks. In this scenario, the envelope radius could extend to $R_{\text{env}} \sim 10^{18}$ cm before merging with the ISM (Yuan et al. 2020, 2021). In the subsequent subsections, we adopt $k = 1.8$ and $R_{\text{env}} = 10^{18}$ cm as fiducial parameters and model the dynamics of jets using n_{ext} defined in Eq. 3. We will demonstrate in the following subsections that within the data-fitting time window, the fast and slow jets propagate, respectively, in the ISM (e.g., $R_f > R_{\text{env}}$) and the envelope (e.g., $R_s < R_{\text{env}}$).

Before delving into the kinetic equations for the jets, let us first parameterize the power converted to the fast and slow outflows from accretion using the energy conversion efficiency η_f and η_s ,

$$L_{f/s} = \eta_{f/s} \dot{M}_{\text{BH}} c^2, \quad (4)$$

where $\eta_{f/s} \sim \mathcal{O}(0.1)$ represents the fraction of the accreted power is converted to jet.

3.2. Jet evolution with continuous energy injection

We follow the methodology for blastwave dynamics, as in the diagram of GRB afterglow modeling (Nava et al.

2013; Zhang 2018; Zhang et al. 2023), to derive the differential equations governing the evolution of the jet, incorporating time-dependent energy and mass injections. For the fast jet initial Lorentz factor $\Gamma_{f0} \sim \mathcal{O}(10)$ to be used in the multiwavelength modeling, we estimate the early-time fast jet radius in the order of

$$R_f \sim \frac{2\Gamma_{f0}^2 c T_{\text{obs}}}{1+z} \simeq 2.1 \times 10^{18} \text{ cm} \left(\frac{\Gamma_{f0}}{30}\right)^2 \left(\frac{T_{\text{obs}}}{1 \text{ d}}\right), \quad (5)$$

which is larger than R_{env} and implies the fast jet is propagating inside the ISM in the time window for lightcurve and SED fitting, e.g., $T_{\text{obs}} \gtrsim 10$ d. We will show later in this section that the slow jet with initial Lorentz factor $\Gamma_{s0} \sim 5$ will decelerate inside the circumnuclear material for $T_{\text{obs}} \lesssim 100$ d. For both jets, we ignore the adiabatic cooling of the jet as it becomes important only when the density profile index $k \geq 3$ is used (see Nava et al. 2013; Zhang 2018, for details).

Let's consider a general case where the jet of initial Lorentz factor Γ_0 penetrates deeply into the ambient gaseous medium. The jet sweeps up material, resulting in the formation of a forward shock (FS) that accelerates the upstream ISM to the Lorentz factor $\Gamma \lesssim \Gamma_0$, and a reverse shock that decelerates the unshocked ejecta from an initial Lorentz factor Γ_0 to Γ . Fig. 5 schematically shows the geometry of the forward shock, reverse shock and the discontinuity between their downstreams. We consider a simplified case that neglects the impact of the reverse shock (RS) on jet evolution. A comprehensive treatment incorporating the reverse shock and a justification for this simplification is provided in Appendix A.

We utilize the fast jet as an exemplar to derive the differential equations describing the jet's evolution. Adopting the approach used in external shock models for GRB afterglow modeling (e.g., Huang et al. 1999; Pe'er 2012; Nava et al. 2013) and neglecting the radiative cooling, we express the total isotropic-equivalent energy of the relativistic jet as

$$\mathcal{E}_{f,\text{iso}} = \Gamma_f M_{\text{ej}} c^2 + \Gamma_f m_{\text{ext}} c^2 + \Gamma_{f,\text{eff}} \mathcal{E}'_{f,\text{int}}, \quad (6)$$

where M_{ej} represents the isotropic-equivalent ejecta mass, m_{ext} is the external mass swept by the outflow, $\mathcal{E}'_{f,\text{int}} = (\Gamma_f - 1)m_{\text{ext}} c^2$ represents the internal energy of the shocked material (downstream) in the jet comoving frame, $\Gamma_{f,\text{eff}} = (\hat{\gamma}\Gamma_f^2 - \hat{\gamma} + 1)/\Gamma_f$ is the effective Lorentz factor and $\hat{\gamma} = (4 + \Gamma_f^{-1})/3$ is the adiabatic index taking into account the transition from relativistic to mild-relativistic. Noting the continuous energy and mass injections and the propagation of the outflow, we explicitly write down

$$M_{\text{ej}} = \int dt \frac{L_{f,\text{iso}}}{\Gamma_{f0} c^2}, \quad m_{\text{ext}} = \int 4\pi R_f^2 m_p n_{\text{ext}} dR_f, \quad (7)$$

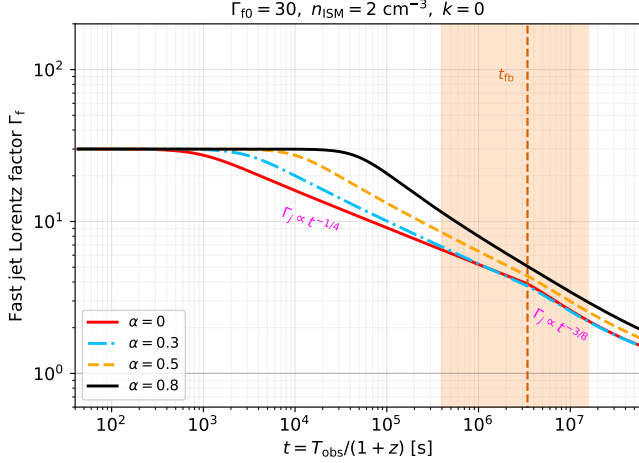


Figure 2. Test time evolution of fast jet Lorentz factor with persistent power and mass injections for the simple case $k = 0$. From the thin red curve to the thick black curve, α varies from 0 to 0.8. The vertical orange dashed line shows the fallback time, whereas the orange area represents the time window ($10 \text{ d} \lesssim T_{\text{obs}} \lesssim 400 \text{ d}$) for X-ray and radio data fitting.

where $L_{f,\text{iso}} = L_f/(\theta_f^2/2)$ is the isotropic jet luminosity given the jet opening angle θ_f , and Γ_{f0} is the jet initial Lorentz factor before deceleration. From the perspective of energy conservation, the change of $\mathcal{E}_{f,\text{iso}}$ is

$$d\mathcal{E}_{f,\text{iso}} = c^2 dm_{\text{ext}} + L_{f,\text{iso}} dt. \quad (8)$$

In this expression, the first term accounts for the energy by accumulating external mass into the jet whereas the second component demonstrates the persistent energy injection from the central engine.

Combining Eqs. 6, 7 and 8, we obtain the differential equation for the jet deceleration

$$\frac{d\Gamma_f}{dm_{\text{ext}}} = -\frac{4\Gamma_f^5 - (5 + 3A_{\text{inj}})\Gamma_f^3 + \Gamma_f}{3M_{\text{ej}}\Gamma_f^3 - 2m_{\text{ext}} + 8\Gamma_f^4 m_{\text{ext}}}, \quad (9)$$

which resembles the formulation for GRBs (e.g., Zhang et al. 2021), with the exception of an additional correction factor arising from continuous energy and mass injection,

$$A_{\text{inj}} = \left(1 - \frac{\Gamma_f}{\Gamma_{f0}}\right) \frac{L_{f,\text{iso}}}{c^2} \left(\frac{dm_{\text{ext}}}{dt}\right)^{-1}. \quad (10)$$

To numerically solve Eq. 9, we connect the jet radius to the SMBH-rest frame time t , e.g.,

$$dR_f = \frac{\beta_f c dt}{1 - \beta_f} \approx 2\Gamma_f^2 \beta_j c dt, \quad (11)$$

where $\beta_f = \sqrt{1 - \Gamma_f^{-2}}$.

To test the impact of time-dependent power injection rates, we show in Fig. 2 the time evolution of jet Lorentz factor using the simple density profile with $k = 0$ and $n_{\text{ISM}} = 2 \text{ cm}^{-3}$ for the fast jet case. We fix the initial jet Lorentz factor to be $\Gamma_{f0} = 30$ and use the values $\eta_f = 0.12$ and $\theta_f = 0.15$ obtained from the X-ray data fitting in Sec. 4. From thin red curve to the thick black curve, the parameter α varies from 0 to 0.8. The vertical orange dashed line depicts the fallback time whereas the yellow area represents the time window of the X-ray and radio data to be fitted. Initially, the external mass m_{ext} is not high enough to decelerate the jet and the Lorentz factor remains a constant level, known as the ‘coasting phase’. The deceleration occurs at t_{dec} when $M_{\text{ej}}/\Gamma_{f0} \simeq m_{\text{ext}}$ is satisfied. The decaying slope of Γ_f before t_{fb} for each curve in Fig. 2 aligns well with the theoretical estimation $\Gamma_f \propto t^{-(2+\alpha)/8}$ derived from $\int L_{f,\text{iso}} dt \sim 4\pi R_f^3 \Gamma_f^2 m_p c^2/3$. In this regime, we find the correction factor to be $A_{\text{inj}} \lesssim 0.1$. The increasing M_{ej} primarily leads to the modifications from the continuous injection.

For $t > t_{\text{fb}}$, the energy injection rate decays much faster and the Γ_f enters the Blandford-McKee (BM) self-similar regime (Blandford & McKee 1976), e.g., the $\Gamma_f \propto R_f^{-2/3} \propto t^{-3/8}$, predicted by a fixed $\mathcal{E}_{f,\text{iso}} \sim 4\pi R_f^3 \Gamma_f^2 n_{\text{ext}} m_p c^2/3$. In this picture, we typically expect two break points at t_{dec} and t_{fb} , similar to the red curve in Fig. 2. However, for a larger α , t_{dec} becomes closer to t_{fb} and the decaying slope $(2 + \alpha)/8$ approaches to $3/8$, which as a result makes the second break at t_{fb} less prominent. We also observe that $\Gamma_f(t)$ is very sensitive to α as it approaches to 1.

The derivation presented above is also applicable to slow jets by substituting the corresponding physical quantities with those for slow jets., e.g., Γ_s, L_s and θ_s . For a slow jet with $\Gamma_{s0} = 4$, we estimate the deceleration time $t_{\text{dec},s} \sim 0.7 \text{ d}$ using

$$\int L_{s,\text{iso}} dt = \frac{4\pi}{3-k} \Gamma_{s0}^2 m_p n_{\text{ext}} (R_s) R_s^3 c^2 \quad (12)$$

and the radius $R_s \approx 2\Gamma_{s0}^2 ct$. We can also estimate the slow jet radius at $T_{\text{obs}} = 100 \text{ d}$ to be $R_s \lesssim R_{\text{env}}$ which implies that the slow jet is propagating within the circumnuclear medium characterized by the index $k = 1.8$.

So far, we have derived the differential equations for TDE jet evolution, taking in to account the continuous injection rate defined in Eq. 1 and Eq. 4. In Sec. 4, we will apply this model to both fast and slow jets with different initial conditions and jet parameters. Subsequently, we will compute the synchrotron and inverse Compton emissions in their respective forward shock and reverse shock regions.

4. MULTIZONE AND MULTIWAVELENGTH MODELING

In this section, we model the emissions from the forward and reverse shocks for both fast and slow jets. We apply the structured jet model to fit the X-ray (0.3–10 keV) and radio/millimeter (15.5 GHz and 225 GHz) lightcurves and spectra. We use two sets of jet parameters ($\eta_f, \theta_f, \Gamma_{f0}$) and ($\eta_s, \theta_s, \Gamma_{s0}$) to describe the time evolutions of the fast and slow jets, as summarized in Table 1.

Regarding the thermal optical emissions, which may stem from the accretion disk or a hot corona, we consider them as upper limits within the multizone model.

4.1. Jet forward shock and reverse shock modeling

For simplicity, we continue using the fast jet as an example, noting that the forward and reverse shock models presented here are also applicable to slow jets by substituting the corresponding physical quantities with those for slow jets.

Forward shock (FS) – In the jet forward shock model, given the external particle number density n_{ext} and Γ_f , we parameterize the magnetic field strength of the downstream magnetic field as $B_{f,\text{fs}} = [32\pi\Gamma_f(\Gamma_f - 1)\epsilon_B^{\text{fs}}n_{\text{ISM}}m_p c^2]^{1/2}$, where ϵ_B^{fs} represents the fraction of internal energy density that goes into the magnetic field energy density. We consider the shock-accelerated nonthermal electrons, described by a power-law injection rate, e.g., $\dot{Q}_{e,\text{fs}}(\gamma_e) \propto \gamma_e^{-s}$, where γ_e is the electron Lorentz factor and $s \geq 2.0$ is the spectral index. To normalize the injection rate, we introduce the number fraction (f_e^{fs}) of the downstream electrons that are accelerated and the energy fraction (ϵ_e^{fs}) of the internal energy that are deposited to nonthermal electrons. In this approach, we infer the minimum Lorentz factor for injected electrons,

$$\gamma_{e,m}^{\text{fs}} = (\Gamma_f - 1)g(s)\frac{\epsilon_e^{\text{fs}} m_p}{f_e^{\text{fs}} m_e}, \quad (13)$$

where $g(s) = (s-2)/(s-1)$ for $s > 2.0$ and $g(s) \sim \mathcal{O}(0.1)$ for $s = 2.0$. We then normalize $\dot{Q}_{e,\text{fs}}$ via

$$(4\pi R_f^2 t'_{f,\text{dyn}} c) \int \dot{Q}_{e,\text{fs}} d\gamma_e = \frac{4\pi f_e^{\text{fs}} R_f^3 n_{\text{ext}}}{3t'_{f,\text{dyn}}}, \quad (14)$$

where $t'_{f,\text{dyn}} = R_f/(\Gamma_f c)$ is the dynamic time measured in the comoving frame.

Reverse shock (RS) – For the reverse shock, we parameterize the magnetic field strength and electron injection rate for the reverse shocks, e.g., $B_{f,\text{rs}}$ and $\dot{Q}_{e,\text{rs}}$. In contrast to the forward shock scheme, the relative Lorentz factor between reverse shock up and

Table 1. Physical (fiducial and fitting) parameters for the structured jet model

Category	Parameter	Value
Fiducial	M_{BH}	$10^7 M_\odot$
	M_\star	$5 M_\odot$
	η_{acc}	0.1
Fitting parameters		
Universal	α	0.8
	n_{ISM}	2.0 cm^{-3}
	R_{env}	10^{18} cm
	k	1.8
	s	2.3
Fast, slow jets	$\eta_{f,s}$	0.12, 0.04
	$\theta_{f,s}$	0.15, 0.3
	$\Gamma_{f0,s0}$	30, 4.0
FS, RS	$\epsilon_e^{\text{fs,rs}}$	0.1, 0.2
	$\epsilon_B^{\text{fs,rs}}$	$3.0 \times 10^{-3}, 0.1$
	$f_e^{\text{fs,rs}}$	$1.0, 1.5 \times 10^{-3}$

downstreams is $\Gamma_{f,\text{rs-rel}} \approx (\Gamma_{f0}/\Gamma_f + \Gamma_f/\Gamma_{f0})/2$. Similar to the forward shock case, we define the reverse shock parameters ϵ_e^{rs} , f_e^{rs} , and ϵ_B^{rs} . In this case, the magnetic field strength of the reverse shock region can be written as

$$B_{f,\text{rs}} = \sqrt{32\pi\epsilon_B^{\text{rs}}\Gamma_{f,\text{rs-rel}}(\Gamma_{f,\text{rs-rel}} - 1)n'_{f,\text{rs}}m_p c^2}, \quad (15)$$

where $n'_{f,\text{rs}} = L_{f,\text{iso}}/(4\pi\Gamma_{f0}^2 R_f^2 m_p c^3)$ is the comoving upstream number density of the reverse shock. The minimum Lorentz factor of injected electrons in reverse shocks, e.g., $\gamma_{e,m}^{\text{rs}}$ can be obtained by replacing Γ_f with $\Gamma_{f,\text{rs-rel}}$ in Eq. 13. Moreover, the particle number injection rate $\dot{N}_{\text{rs}} = L_{f,\text{iso}}/(\Gamma_{f0} m_p c^2)$ should be used to normalize $\dot{Q}_{e,\text{rs}}$, which can be expressed explicitly as

$$(4\pi R_f^2 t'_{f,\text{dyn}} c) \int \dot{Q}_{e,\text{rs}} d\gamma_e = f_e^{\text{rs}} \dot{N}_{\text{rs}} = \frac{f_e^{\text{rs}} L_{f,\text{iso}}}{\Gamma_{f0} m_p c^2}. \quad (16)$$

Given the injected electron rates and the magnetic fields in forward and reverse shocks, we use the AM³ software (Klinger et al. 2023) to model the synchrotron and synchrotron self-Compton emissions in these two regions by numerically solving the corresponding time-dependent transport equations for electrons in the comoving frame,

$$\frac{\partial n'_e}{\partial t'} = \dot{Q}_e - \frac{\partial}{\partial \gamma_e} (\dot{\gamma}_e n'_e) - \frac{n'_e}{t'_{f,\text{dyn}}}. \quad (17)$$

In this equation, n'_e and t' represents the electron number density (differential in Lorentz factor and vol-

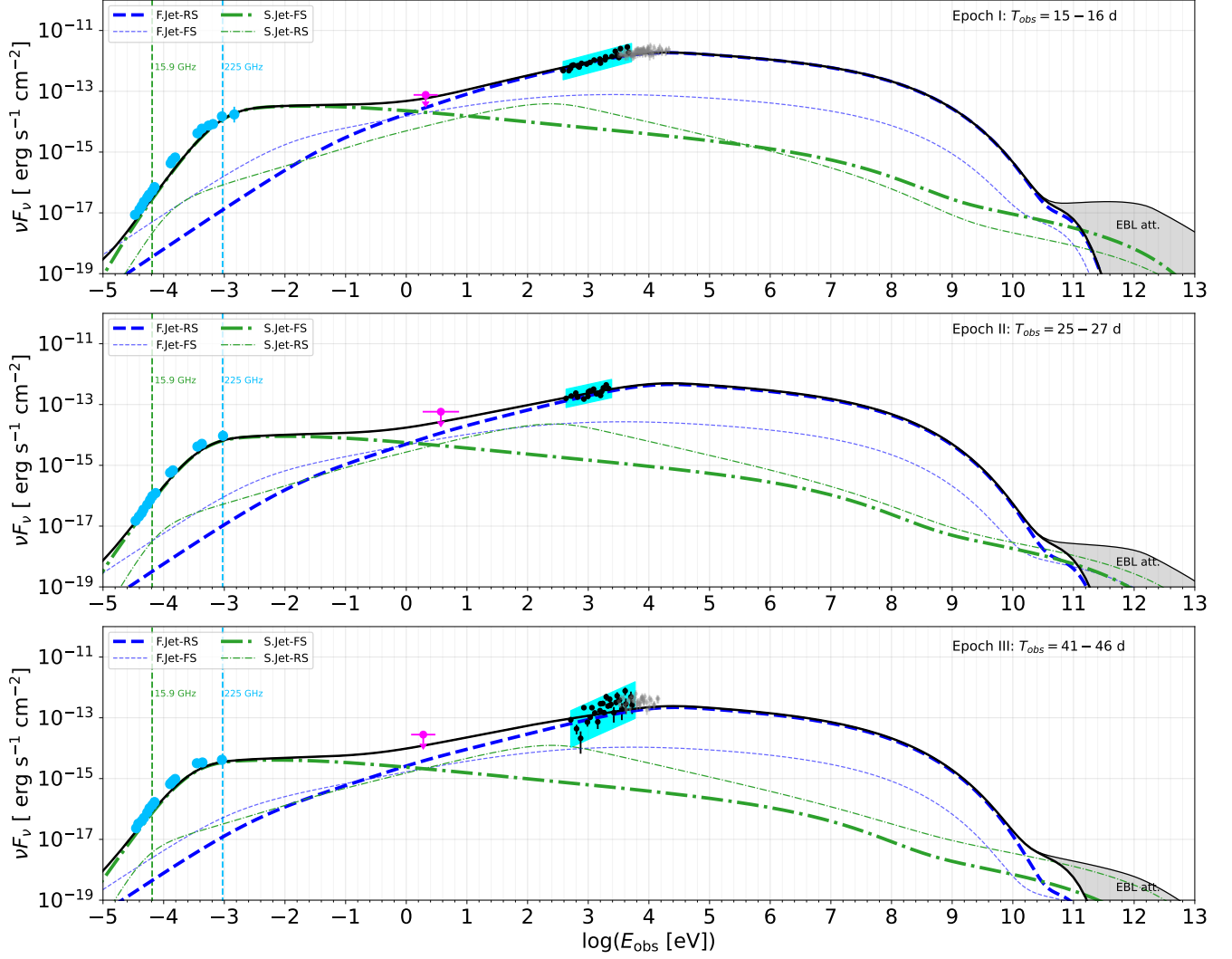


Figure 3. Spectral fitting for three epochs. The ‘SY/IC’ spectra of the fast/slow jet forward (F.Jet/S.Jet-FS) and reverse shocks (F.Jet/S.Jet-RS), are illustrated. The magenta points depict the energy fluxes in optical bands, which are considered as the upper limits. The thin and thick solid black curves correspond to the overall SED before and after applying $\gamma\gamma$ attenuation with EBL. The radio/millimeter and X-ray data are depicted as blue and black dots, respectively (Andreoni et al. 2022; Pasham et al. 2023). Additionally, the hard X-ray energy fluxes (Yao et al. 2024) are also shown as gray points.

ume) and time measured in jet comoving frame, $\dot{\gamma}_e \sim \gamma_e(t'_{e,\text{sy}}^{-1} + t'_{e,\text{ic}}^{-1})$ is the electron energy loss rate due to synchrotron and inverse Compton radiation in the synchrotron self-Compton diagram. In addition, we self-consistently estimate the electron maximum Lorentz factor by balancing the efficient acceleration rate $t'_{e,\text{acc}}^{-1} \sim eB_f/(\gamma_e m_e c)$ and the cooling rate $t'_{e,c}^{-1} = t'_{e,\text{sy}}^{-1} + t'_{e,\text{ic}}^{-1}$. To get the observed photon spectra, we convert the obtained comoving photon density spectrum $n'_\gamma = d^2 N_\gamma / (d \ln E'_\gamma dV')$ in the units of cm^{-3} to the flux in the observer’s frame via

$$\nu F_\nu(E_{\gamma,\text{obs}}) = f_{\text{br}} \Gamma_f^2 \left(\frac{R_f^2}{d_L^2} \right) c E'_\gamma n'_\gamma \exp(-\tau_{\text{EBL}}), \quad (18)$$

where the observed and comoving energies are connected by $E_{\gamma,\text{obs}} = \Gamma_f E'_\gamma / (1+z)$, $f_{\text{br}} = 1/[1 + (\Gamma_f \theta_f)^{-2}]$ accounts for the jet break correction, and we also applied the correction of $\gamma\gamma$ absorption attributed to the attenuation with extragalactic background light (EBL) during propagating from $z = 1.19$ ($d_L \simeq 8.4$ Gpc) to the Earth.

4.2. Fast jet: X-ray data fitting

We apply the dynamics of the fast and slow jet (Sec. 3.2) together with the modeling of the forward and reverse shocks to explain the measured 0.3-10 keV lightcurve and the X-ray spectra in multiple epochs (Andreoni et al. 2022; Pasham et al. 2023; Yao et al. 2024), e.g., $T_{\text{obs}} = 15 - 16$ d, $25 - 27$ d, $41 - 46$ d. To reduce the free parameters, we assume the forward shocks

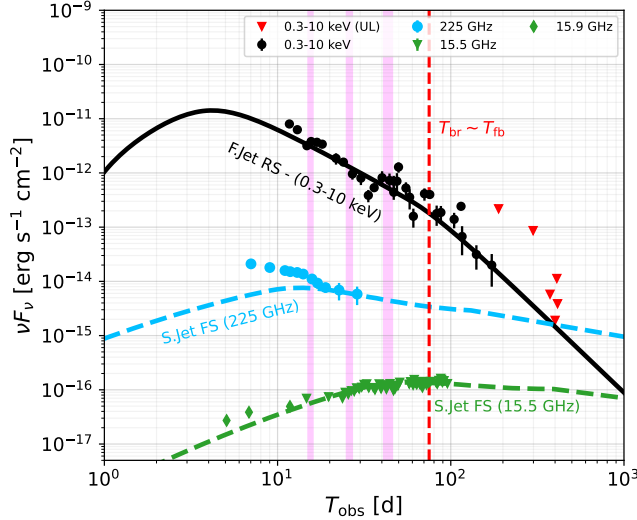


Figure 4. Fitting of nonthermal X-ray and radio lightcurves using the parameters in Table 1. The solid black line represents the 0.3-10 keV X-ray afterglow from the fast jet’s reverse shock model (F.Jet RS). The blue and green dashed curves depict the 225 GHz and 15.9 GHz lightcurves obtained from the slow jet forward shock (S.Jet FS) scenario. The vertical magenta areas represent the three epochs for SED fitting in Fig. 3. The latest X-ray upper limits (ULs) are depicted as red triangles. The vertical red line represents the fast jet break time (T_{br}), which is close to the fallback time (T_{fb}). Data sources: Andreoni et al. (2022); Pasham et al. (2023); Yao et al. (2024); Eftekhari et al. (2024)

of the fast and slow jets share the same ϵ_e^{fs} , ϵ_B^{fs} and f_e^{fs} , whereas all reverse shocks have the same ϵ_e^{rs} , ϵ_B^{rs} and f_e^{rs} .

We fix the spectral index of injected electrons to be $s = 2.3$ during our calculation. The fiducial parameters for the TDE accretions and the external density profile, together with the physical parameters of the jets and the reverse/forward shocks obtained by fitting the X-ray and radio/millimeter spectra and lightcurve, are presented in Table 1.

Fig. 3 shows the fitting to the SED in three epochs, $T_{\text{obs}} = 12 - 15$ d, $25 - 27$ d, $41 - 46$ d, respectively in the top, middle and bottom panels. The X-ray (black points), optical (magenta points), and radio/millimeter (blue points) are sourced from Andreoni et al. (2022); Pasham et al. (2023), whereas the hard X-ray data (gray points, Yao et al. 2024) at the closest observation windows are also shown. In the fast jet (denoted as ‘F.Jet’) scenario, the thin and thick blue dashed curves depict the combined synchrotron and inverse Compton (denoted as ‘SY/IC’) emissions from the forward shock (FS) and reverse shock (RS) regions. From this figure, we find that, by adopting the parameters in Table 1, the reverse shock fast-cooling synchrotron spectra are con-

sistent with the observed X-ray data. We also observe that the forward shock is subdominant using the parameters for radio data fitting. The forward shock and reverse shock spectra are also consistent with the analytical predictions in Appendix B.

In Fig. 4, we present the fitting to the measured X-ray lightcurve (Yao et al. 2024) using the jet scenario. Our results indicate that emissions from the fast jet reverse shock could account for the fast-decaying X-ray lightcurve, since the decaying accretion rate defined in Eq. 1 can directly influence the injection rate of the accelerated electrons. As we observed that the forward shock is sub-dominant in the X-ray bands and predicts a more flat lightcurve, its lightcurve is not displayed in this figure.

To comprehend the temporal evolution of these regions, we derive the analytical X-ray lightcurves considering the time-dependent energy injection luminosity before and after the fallback time. Requiring $\Gamma_f = 1/\theta_f$, we infer the fast jet break time to be $t_{\text{br}} \simeq 2.8 \times 10^6$ s for $\theta_f = 0.15$, which is close to the fallback time t_{fb} . For simplicity, in the following discussions, we do not distinguish t_{fb} and t_{br} , and treat the jet as post-break and apply the steepening factor $f_{\text{br}} = (\Gamma_f \theta_f)^2 \propto T_{\text{obs}}^{-3/4}$ to the lightcurve after t_{fb} . In this case, the analytical X-ray lightcurves for both forward and reverse shocks in the fast cooling regime can be written respectively as

$$\nu F_\nu^{(\text{fs})} \propto \begin{cases} f_{\text{br}} T_{\text{obs}}^{-\alpha+1-s/2}, & T_{\text{obs}} < T_{\text{br}} \simeq T_{\text{fb}} \\ f_{\text{br}} T_{\text{obs}}^{-1}, & T_{\text{obs}} > T_{\text{br}} \simeq T_{\text{fb}}, \end{cases} \quad (19)$$

and

$$\nu F_\nu^{(\text{rs})} \propto \begin{cases} T_{\text{obs}}^{-[5\alpha+\alpha(s-1)]/4}, & T_{\text{obs}} < T_{\text{br}} \simeq T_{\text{fb}} \\ T_{\text{obs}}^{-(2s+25)/12}, & T_{\text{obs}} > T_{\text{br}} \simeq T_{\text{fb}}. \end{cases} \quad (20)$$

where $T_{\text{br}} = (1+z)t_{\text{br}}$, $T_{\text{fb}} = (1+z)t_{\text{fb}}$, and a detailed derivation is provided in Appendix B. They are consistent with the GRB afterglow lightcurves for both forward shocks and reverse shocks (see Zhang 2018, for details). Since we adopted the approximations, $\Gamma_{f,\text{rs-rel}} \sim \Gamma_{f,\text{rs-rel}} - 1 \sim \Gamma_{f0}/(2\Gamma_f)$, to obtain Eq. 20, the numerical time decay slope could be steeper by a correction factor $\sim T_{\text{obs}}^{-0.2} - T_{\text{obs}}^{-0.4}$. The analytical lightcurves closely match the numerical results obtained using $\alpha = 0.8$ in Fig. 4. Specifically, the jet break time in the observer’s frame, $T_{\text{br}} \simeq 72$ d, and the steepened temporal evolution for $s = 2.3$, such as $\propto T_{\text{obs}}^{-2.7} - T_{\text{obs}}^{-2.9}$, after T_{br} , are consistent with the X-ray fluxes in the time window $T_{\text{br}} < T_{\text{obs}} < 200$ d and the late-time upper limits (illustrated as red triangles, Eftekhari et al. 2024) extending to $T_{\text{obs}} \sim 400$ d. Conversely, the forward shock is dis-

avored due to its relatively flat temporal evolution and negligible flux in X-ray bands.

4.3. Slow jet: radio/millimeter data fitting

Recently, Matsumoto & Metzger (2023), Yao et al. (2024), and Zhou et al. (2024) demonstrated that jet forward shocks, similar to those in GRB afterglow models, can interpret the radio observations of AT 2022cmc. The radio spectra and light curves are well described by a decelerated, mildly relativistic jet with an initial Lorentz factor of $\sim 3 - 10$ in a circumnuclear medium characterized by an index of $1.5 \lesssim k \lesssim 2$. In this work, we aim to provide a more comprehensive model of the multiwavelength emissions from jetted TDEs by considering a slow jet (in addition to the fast jet used for X-ray data fitting) propagating within R_{env} . This approach is consistent with previous studies. The major difference in our work is the inclusion of persistent energy injection due to long-lasting accretion activities, as discussed in Sec. 3.2.

Similar to the fast jet scenarios, we self-consistently compute the time-dependent synchrotron and inverse Compton emissions in the forward shock and reverse shock regions, as discussed in Sec. 4.1. By fitting the radio observations, we obtain the slow jet parameters (η_s , θ_s , and Γ_{s0}) and the forward shock parameters (ϵ_e^{fs} , ϵ_B^{fs} and f_e^{fs}), as summarized in Table 1. Comparing to the fast $\Gamma_{f0} = 30$ and narrow ($\theta_s = 0.15$) jet considered in Sec. 4.3, a slow ($\Gamma_{s0} = 4$) and wide ($\theta_s = 0.3$) jet is favored to fit the radio data. For completeness, we incorporate the reverse shock parameters obtained from X-ray data fitting in the fast jet scenario to account for the contribution from the slow jet reverse shock regions.

The fitted forward shock SY/IC spectra in the slow jet scenario are shown as the thick green dashed-dotted curves in Fig. 3 together with the observed radio/millimeter SED (blue points) and the reverse shock components (thin green dashed-dotted curves). In Fig. 4, we also compare our model-predicted 15.5 GHz (green curve) and 225 GHz (blue curve) lightcurves with the corresponding observations. Our results demonstrate that the forward shock of the continuously powered slow jet can reproduce the observed radio/millimeter spectra and lightcurves. Our results and parameters are consistent with Matsumoto & Metzger (2023), and the cumulative slow jet energy

$$\mathcal{E}_{\text{s,iso}} = \frac{2\eta_s \dot{M}_{\text{BH}}(t_{\text{fb}}) c^2 t_{\text{fb}}}{(1 - \alpha)\theta_s^2} \sim 8 \times 10^{53} \text{ erg}. \quad (21)$$

To understand the radio spectra fitting, we estimate the synchrotron characteristic frequency and the cooling

frequency in the forward shock region to be respectively,

$$\nu_m = \frac{3\Gamma_s(\gamma_{e,m}^{\text{fs}})^2 e B_{s,\text{fs}}}{4\pi(1+z)m_e c} \simeq 3.8 \times 10^2 \text{ GHz} \times \left(\frac{T_{\text{obs}}}{15 \text{ d}}\right)^{-0.9} \left(\frac{\Gamma_s}{3}\right)^{2.2} \quad (22)$$

and

$$\nu_c = \frac{3\Gamma_s \gamma_{e,c}^2 e B_{s,\text{fs}}}{4\pi(1+z)m_e c} \simeq 3.1 \times 10^4 \text{ GHz} \times \left(\frac{T_{\text{obs}}}{15 \text{ d}}\right)^{0.7} \left(\frac{\Gamma_s}{3}\right)^{1.4}, \quad (23)$$

where $\gamma_{e,c} \sim 6\pi m_e c / (\sigma_T B_{s,\text{fs}}^2 \Gamma_s t)$ is the electron cooling Lorentz factor and σ_T is the Thomson cross section. The wind SY/IC spectra in Fig. 3 are consistent with the weak synchrotron self-absorption (SSA) in the electron slow-cooling regime, e.g., the absorption frequency $\nu_a < \nu_m < \nu_c$, characterized by a steep increasing tail, e.g., $\nu F_\nu \propto \nu^3$ for $\nu < \nu_a$. Another mechanism that may prevent the radio emission to escape is the free-free absorption due to the thermal electrons in the external medium, which typically requires very high n_{ext} . Applying Eq. 3, we find that the free-free optical depth, $\tau_{\text{ff}} \propto n_{\text{ext}}^2$ (e.g., Murase et al. 2017), is extremely low, and conclude that this effect is negligible in radio data fitting.

The slow jet forward shock model can explain the 225 GHz and 15.5 GHz fluxes and lightcurves very well after $T_{\text{obs}} = 15 \text{ d}$. However, the early stage radio/millimeter fluxes for $T_{\text{obs}} < 15 \text{ d}$ are underestimated by the slow jet forward shock model, as illustrated in Fig. 4. This suggests that the early-time radio emissions may originate from different zones, such as structured two-component outflows (Zhou et al. 2024; Sato et al. 2024), or may be contaminated by the accretion disks. Regarding the slow jet reverse shock component, the use of a very small f_e^{rs} results in a very high minimum Lorentz factor for the accelerated electrons. Consequently, the corresponding SY/IC spectra peak at much higher energies compared to the forward shock case, e.g., the thin green dashed-dotted curves in Fig. 3, and the reverse shock contribution to the radio/millimeter energy fluxes is minimal.

Overall SEDs – We have presented a comprehensive discussion of the forward shock and reverse shock components in the fast and slow jets. Combining the emissions from these zones, we obtain the overall SED for the three epochs before and after applying the EBL absorption. These are respectively represented by the thin and thick black solid curves in Fig. 3. For reference, the thermal optical data (magenta points) are also included as the upper limits. The limited contribution

of the jets to the optical bands is consistent with optical observations. Importantly, our multizone model, incorporating the forward and reverse shocks of both fast and slow jets, effectively describes multi-wavelength observations, encompassing radio and X-ray spectra, along with their corresponding lightcurves.

5. DISCUSSION

We have analyzed both forward shock and reverse shock scenarios for both fast and slow jets, identifying the reverse shock of the fast jet and the forward shock of the slow jet regions as promising X-ray and radio sources for the jetted TDE AT 2022cmc. Their primary advantages are summarized below:

- **Fast jet reverse shock:** The combination of continuously decaying energy injection and deceleration in the ISM leads to a rapidly decaying X-ray lightcurve, consistent with observations. However, one caveat is that fitting the spectra requires a very low value of $f_e^{\text{rs}} = 1.5 \times 10^{-3}$.
- **Slow jet forward shock:** The typical values of $\epsilon_B^{\text{fs}} = 3.0 \times 10^{-3}$ and $f_e^{\text{fs}} = 1$, consistent with GRB afterglow modeling, along with the presence of a dense external medium, facilitate the consistency of SSA with the radio spectra. Additionally, the radio/millimeter lightcurves can be effectively modeled by the deceleration of the jet within the circumnuclear medium ($R_s \lesssim R_{\text{env}}$).

Mass of the disrupted star – To construct the accretion history of AT 2022cmc, we initially assume a disrupted star of $5 M_\odot$ in Eq. 1. A lower limit for M_\star can be estimated based on the isotropic equivalent X-ray luminosity, e.g., $L_{X,\text{iso}} \sim 3 \times 10^{47} \text{ erg s}^{-1} (T_{\text{obs}}/5 \text{ d})^{-2}$ (Andreoni et al. 2022), which implies an X-ray energy $E_{X,\text{iso}} \gtrsim 1.3 \times 10^{53} \text{ erg}$. Using the energy conversion efficiencies, the mass of the disrupted star can be estimated as

$$M_\star \sim \frac{2f_{\text{bol}}f_b E_{X,\text{iso}}}{\eta_{\text{acc}}\eta_f \epsilon_e^{\text{fs}} c^2} \gtrsim 3.3 M_\odot \eta_{\text{acc},-1}^{-1} \eta_f^{-1}, \quad (24)$$

where $f_{\text{bol}} \sim 3 - 4$ is bolometric correction factor and $f_b = \theta_f^2/2$ is the jet beaming factor. Additionally, when lower accretion and jet efficiencies are used, a significantly more massive star is needed to explain the bright X-ray emissions. As a result, the likelihood of such disruptions would decrease notably. Thus, our fiducial values for M_\star , η_{acc} , and η_f are reasonable rather than optimistic within the context of this work.

X-ray variability – In addition to its rapid decay, another significant feature of the observed X-ray lightcurve is its rapid variability, characterized by a timescale of

$\Delta T_{\text{var}} \sim 10^3 \text{ s}$ (Yao et al. 2024). However, since we assume a homogeneous reverse shock downstream without considering the small scale plasma fluctuations, the intrinsic variability time scale of the reverse shock is much longer than ΔT_{var}

$$\Delta T_{\text{var,rs}} = (1+z) \frac{R_f}{\Gamma_f^2 \beta_f c} \sim T_{\text{obs}} \gg 10^3 \text{ s}. \quad (25)$$

This indicates that the fast variability cannot be attributed solely to the fast jet reverse shock region. In the reverse shock scenario, since the central engine is active, afterglow variabilities might arise when late-time outflow from the central engine collides with the preceding blast wave, resulting in a variability timescale down to the light crossing time of the central engine (Ioka et al. 2005). Furthermore, the physical characteristics of the reverse shock region depend sensitively on $L_{f,\text{iso}}$, which can be modulated by accretion at the horizon of the SMBH (Reis et al. 2012), leading to rapid variations on the timescale $\Delta T_{\text{var,eng}} \sim (1+z)R_{\text{Sch}}/c \sim 10^3 \text{ s}$, where R_{Sch} is the Schwarzschild radius. Overall, the continuously powered reverse shock scenario predicts both long-term (e.g., $\Delta T_{\text{var,rs}}$) and rapid (e.g., $\Delta T_{\text{var,eng}}$) X-ray variabilities, stemming from the reverse shock downstream and the central engine, respectively.

Late-time X-ray upper limits – Recently, Eftekhari et al. (2024) reported the late-time X-ray upper limits in 0.3-10 keV band extending to $T_{\text{obs}} \sim 400 \text{ d}$. These upper limits reveal a further steepened X-ray lightcurve, which was interpreted as the cessation of jet activity at $T_{\text{obs}} \sim 215 \text{ d}$, when the accretion rate becomes sub-Eddington. In this paper, we demonstrate that the steepening can also be alternatively explained by the jet break occurred at an earlier time, e.g., $T_{\text{br}} \simeq 72 \text{ d}$. The late-time upper limits and the data points in the time interval $T_{\text{br}} \lesssim T_{\text{obs}} \lesssim 400 \text{ d}$ can be well described by the steepened lightcurve in the jet reverse shock scenario (see Fig. 4).

Radio/millimeter emissions – We show that the radio spectra and lightcurves can be effectively described by the slow jet forward shock regions. However, the model-predicted early-time radio/millimeter energy fluxes fall below the measurements. This issue has also been noted in Zhou et al. (2024); Sato et al. (2024), where additional components or radiation zones are introduced to account for the early-time radio emissions. This suggests that the radio signals of TDEs may have a more complex origin.

γ -ray detectability – Using the same parameters for the jet forward shock, we obtain the energy flux $\nu F_\nu \sim 10^{-14} - 10^{-13} \text{ erg s}^{-1} \text{ cm}^{-2}$ in the *Fermi* Large Area Telescope (LAT) γ -ray band (0.1–10 GeV). The

non-detection of γ -ray sources by *Fermi* within 1° diameter of AT 2022cmc sets an upper limit on the energy flux $\nu F_\nu < 8.8 \times 10^{-9} \text{ erg s}^{-1} \text{ cm}^{-2}$ (Pasham et al. 2023), which is much higher than the γ -ray energy flux predicted by our wind-jet model. Since the forward shock lightcurve maintains a shallow decay before T_{br} , we roughly estimate the 100-day detection horizon for AT 2022cmc-like TDEs for *Fermi*-LAT in the optimistic case as $z \lesssim 0.17$. This corresponds to the occurrence rate of approximately, $\lesssim 0.02 - 0.1 \text{ yr}^{-1}$, using a rate density of $0.02_{-0.01}^{+0.04} \text{ Gpc}^{-3} \text{ yr}^{-1}$ (Andreoni et al. 2022). We infer that, it is difficult for *Fermi* LAT to detect jetted TDE as luminous as AT 2022cmc within one decade, unless a much more efficient energy conversion in the forward shock region is attained.

Multimessenger implication – Since the identification of the first TDE with IceCube neutrino association, AT 2019dsg (Stein et al. 2021), more neutrino-coincident TDE candidates have been identified, such as AT 2019fdr (Reusch et al. 2022), AT 2019aalc (van Velzen et al. 2021), two dust-obscured ones (Jiang et al. 2023), and AT 2021lwx (Yuan et al. 2024). Relativistic jets (Wang & Liu 2016; Dai & Fang 2017; Senno et al. 2017; Lunardini & Winter 2017), sub-relativistic winds (Murase et al. 2020; Liu et al. 2020; Winter & Lunardini 2021, 2023; Mukhopadhyay et al. 2023; Yuan & Winter 2023), and accretion flows (Murase et al. 2020; Hayasaki 2021) have been studied as the origin of the TDE neutrinos. For AT 2022cmc, we have tested the neutrino fluences using an efficient cosmic ray injection in the jet-wind model, where most of the jet power is converted to nonthermal protons. Our results demonstrate a very low neutrino fluence due to the relatively high redshift and less dense target photons, compared to AT 2019dsg, AT 2019fdr, and AT 2019aalc (e.g., Murase et al. 2020; Winter & Lunardini 2023; Yuan & Winter 2023).

6. SUMMARY AND CONCLUSIONS

The distinct signatures of the radio/millimeter, optical/UV and X-ray signals of AT 2022cmc indicate a multi-component origin. In this work, we have presented a time-dependent structured jet model involving a fast relativistic jet (initial Lorentz factor of 30) and a slow relativistic wind (initial Lorentz factor of 4) to explain the multiwavelength spectral and temporal observations of AT 2022cmc. We model the jet evolution within a generic external medium characterized by a power-law density profile, $n_{\text{ext}} \propto R^{-k}$, extending to the ISM. Considering the active central engine powered by continuous accretion characterized by a power-law

decaying accretion rate, we incorporate persistent mass and power injections into the jets, which could significantly affect the dynamics and subsequently the multiwavelength lightcurves before the mass fallback time. For instance, continuous energy and mass injections extend the duration of the reverse shock emissions, enabling the explanation of late-time X-ray observations in the fast jet scenario.

We have self-consistently computed the synchrotron and inverse Compton emissions from the shock-accelerated energetic electrons in the forward and reverse shock regions of the fast and slow jets. We demonstrate that the X-ray spectra and fast decaying lightcurves can be well described by the fast jet reverse shock region, whereas the slow jet forward shock could explain the radio/millimeter observations after $T_{\text{obs}} \sim 10 \text{ d}$. Using the same forward shock parameters and reverse shocks, our calculation demonstrates that the fast jet forward shock and the slow jet reverse shock contributions can be subdominant. Specifically, we observe that the jet forward shock would result in a more shallowly decaying lightcurve. Notably, the fast jet reverse shock X-ray lightcurve steepening due to the jet break at $T_{\text{br}} \simeq 72 \text{ d}$ aligns well with the late-time X-ray energy fluxes and upper limits extending to $T_{\text{obs}} \sim 400 \text{ d}$. Using the same parameters for the jet forward shock region, we estimate the γ -ray energy flux in the energy range 100 MeV to 10 GeV to be $\sim 10^{-14} - 10^{-13} \text{ erg s}^{-1} \text{ cm}^{-2}$ before T_{fb} , which corresponds a detection rate of $\lesssim 0.02 - 0.1$ per year for AT 2022cmc-like jetted TDEs and is consistent with the non-detection of jetted TDEs by *Fermi* LAT. The Klein-Nishina suppression to the inverse Compton emission together with the EBL absorption make it increasingly challenging to be detected in the very-high-energy TeV γ -ray ranges.

Our comprehensive modeling of the structured jet, involving the forward and reverse shock, related to TDEs provides a useful physical framework for interpreting the time-dependent multiwavelength observations of jetted TDEs detected in the future. Meanwhile, this work also provides a prototype to investigate the physical conditions of mass accretion, the ambient gas density profile, and the outflows, through spectral and lightcurve fitting.

ACKNOWLEDGMENTS

We thank Mahmoud Alawashra for the thorough review of the paper. The work of K.M. is supported by the NSF Grant Nos. AST-2108466, AST-2108467, and AST-2308021. B.T.Z. and K.M. are supported by KAKENHI Nos. 20H01901 and 20H05852.

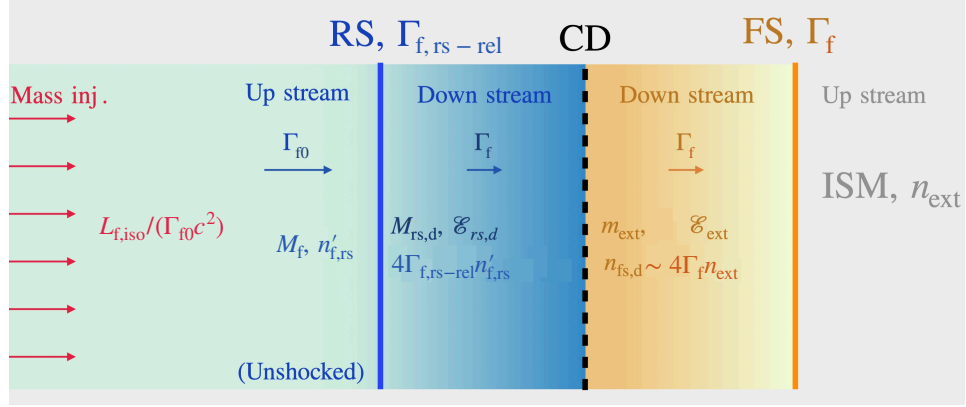


Figure 5. Schematic figure of the fast jet with forward shock (FS), reverse shock (RS) and continuous energy injection. The contact discontinuity (CD) between the reverse shock and forward shock downstreams is also shown. The detailed description of the physical quantities can be found in the text.

APPENDIX

A. EVOLUTION OF RELATIVISTIC JETS WITH CONTINUOUS ENERGY INJECTION: THE FULL TREATMENT WITH FORWARD AND REVERSE SHOCKS

We analyze the evolution of a persistently powered fast jet within an external medium n_{ext} , accounting for the effects of both forward and reverse shocks. Fig. 5 schematically depicts the physical conditions of this jet, including the mass injections, contact discontinuity between the downstreams of reverse shock and forward shock, and the physical quantities (see the text below for the definitions) in different regions. Following the approach used in GRB afterglow modeling (Huang et al. 1999; Pe’er 2012; Nava et al. 2013; Zhang 2018; Zhang et al. 2023), we derive the total energy of the fast jet in the SMBH-rest frame,

$$\mathcal{E}_{f,\text{iso}} = \Gamma_{f0} M_f c^2 + \Gamma_f M_{rs,d} c^2 + \Gamma_{rs,\text{eff}} \mathcal{E}_{rs,\text{in}} + \Gamma_f m_{\text{ext}} c^2 + \Gamma_{fs,\text{eff}} \mathcal{E}_{\text{ext},\text{in}}, \quad (\text{A1})$$

where M_f , $M_{rs,d}$ and m_{ext} are the masses of unshocked ejecta, reverse shock downstream, and the forward shock downstream originated from external medium. The downstream internal energies for forward shock and reverse shock can be written as

$$\begin{aligned} \mathcal{E}_{\text{ext},\text{in}} &= (\Gamma_f - 1) m_{\text{ext}} c^2, \\ \mathcal{E}_{rs,\text{in}} &= (\Gamma_{f,rs-\text{rel}} - 1) M_{rs,d} c^2, \end{aligned} \quad (\text{A2})$$

where $\Gamma_{f,rs-\text{rel}} \approx (\Gamma_f/\Gamma_{f0} + \Gamma_{f0}/\Gamma_f)/2$ is the relative Lorentz factor of the reverse shock and the adiabatic and radiative energy losses are neglected (see Zhang 2018, for details). The effective Lorentz factor are

$$\begin{aligned} \Gamma_{fs,\text{eff}} &= (\hat{\gamma}_{fs} \Gamma_f^2 - \hat{\gamma}_{fs} + 1)/\Gamma_f \\ \Gamma_{rs,\text{eff}} &= (\hat{\gamma}_{rs} \Gamma_f^2 - \hat{\gamma}_{rs} + 1)/\Gamma_f, \end{aligned} \quad (\text{A3})$$

where the adiabatic indices are defined as $\hat{\gamma}_{fs} = (4\Gamma_f + 1)/(3\Gamma_f)$ and $\hat{\gamma}_{rs} = (4\Gamma_{f,rs-\text{rel}} + 1)/(3\Gamma_{f,rs-\text{rel}})$.

Considering the energy injection from the SMBH and the swept-up external material, we have the derivative of $\mathcal{E}_{f,\text{iso}}$

$$d\mathcal{E}_{f,\text{iso}} = c^2 dm_{\text{ext}} + L_{f,\text{iso}} dt. \quad (\text{A4})$$

We obtain the differential equations for Γ_f by combining the equations above,

$$\frac{d\Gamma_f}{dR_f} = - \frac{\overbrace{(\Gamma_{fs,\text{eff}} + 1)(\Gamma_f - 1)c^2 \frac{dm_{\text{ext}}}{dR_f}}^{\text{FS term}} + \overbrace{(\Gamma_f - \Gamma_{f0} - \Gamma_{rs,\text{eff}} + \Gamma_{rs,\text{eff}}\Gamma_{f,rs-\text{rel}})c^2 \frac{dM_{rs,d}}{dR_f}}^{\text{RS term}}}{(M_{rs,d} + m_{\text{ext}})c^2 + \mathcal{E}_{\text{ext},\text{in}} \frac{d\Gamma_{fs,\text{eff}}}{d\Gamma_f} + \mathcal{E}_{rs,\text{in}} \frac{d\Gamma_{rs,\text{eff}}}{d\Gamma_f}}, \quad (\text{A5})$$

where the derivatives of m_{ext} , $M_{\text{rs,d}}$ and M_{f} can be explicitly written as

$$\begin{aligned}\frac{dm_{\text{ext}}}{dR_{\text{f}}} &= 4\pi R_{\text{f}}^2 n_{\text{ext}} m_p, \\ \frac{dM_{\text{rs,d}}}{dR_{\text{f}}} &= \dot{M}_{\text{rs,u}} \left(\frac{dR_{\text{f}}}{dt} \right)^{-1} \\ &= \frac{3M_{\text{f}}c}{R_{\text{f}}} (\beta_{\text{f0}} - \beta_{\text{f}}) \left(\frac{dR_{\text{f}}}{dt} \right)^{-1}, \\ \frac{dM_{\text{f}}}{dt} &= \frac{L_{\text{f,iso}}}{\Gamma_{\text{f0}}c^2} - \frac{3M_{\text{f}}c}{R_{\text{f}}} (\beta_{\text{f0}} - \beta_{\text{f}}).\end{aligned}\tag{A6}$$

In the above expressions, $\beta_{\text{f0}} = \sqrt{1 - \Gamma_{\text{f0}}^{-2}}$ and $\beta_{\text{f}} = \sqrt{1 - \Gamma_{\text{f}}^{-2}}$. Equation A5 is consistent with Eq. A1 in Zhang et al. (2023) and it reduces to the simple Eq. 9 if we neglect the influence of reverse shock by removing the differential terms of reverse shock and letting $M_{\text{rs,d}}$ be the ejecta mass M_{ej} .

To get an intuition of the dominant factors, we observe that the reverse shock term is a high-order correction in Eq. A5 since $(1 - \Gamma_{\text{f}}/\Gamma_{\text{f0}}) \rightarrow 0$, $(\Gamma_{\text{f,rs-rel}} - 1) \rightarrow 0$, and $(\beta_{\text{f0}} - \beta_{\text{f}}) \rightarrow 0$ when the jet is in the coasting regime. Later, in the deceleration stage we infer the ratio

$$\zeta_{\text{rs/fs}} = \frac{\text{RS term}}{\text{FS term}} < \frac{dM_{\text{rs,d}}/dR_{\text{f}}}{dm_{\text{ext}}/dR_{\text{f}}} \lesssim \frac{\bar{n}_{\text{rs}}}{n_{\text{ext}}} \frac{1}{2\Gamma_{\text{f}}^2} \lesssim \frac{3\eta_{\text{f}}\eta_{\text{acc}}M_{\star}}{16\pi\theta_{\text{f}}^2 R_{\text{f}}^3 \Gamma_{\text{f0}} \Gamma_{\text{f}}^2 m_p n_{\text{ext}}},\tag{A7}$$

where $\bar{n}_{\text{rs}} \sim M_{\text{f}}/(4\pi m_p R_{\text{f}}^3/3)$ is the average density of the reverse shock upstream, $M_{\text{f}} \lesssim \int L_{\text{f,iso}} dt / (\Gamma_{\text{f0}} c^2)$, and the definition of $L_{\text{f,iso}}$ are used. Plugging in the fiducial values, we find $\zeta_{\text{rs/fs}} \lesssim 10^{-2}$ for the fast and slow jet within the data-fitting time window, implying that the reverse shock (RS) term in the numerator is negligible. In the denominator, $M_{\text{rs,d}} \approx M_{\text{ej}}$ (ejecta mass in Eq. 9) is satisfied as the reverse shock sufficiently crosses and decelerates the ejecta, thus reducing Eq. A5 to Eq. 9, and we conclude that the reverse shock does not significantly affect the jet evolution. Our calculation also suggests that the reverse shock term may play a role in jet evolution when the jet is exceptionally powerful (with higher $\eta_{\text{f}}\eta_{\text{acc}}M_{\star}$), extremely narrow (with smaller θ_{f}), and compact (with lower Γ_{f0} and R_{f}).

B. ANALYTICAL SOLUTIONS

Here, we take the fast jet as the example to derive the analytical Lorentz factor evolution, and the lightcurves of the forward shock and reverse shock scenarios.

B.1. Jet Lorentz Factor

We firstly derive the fast jet Lorentz factor as a function of T_{obs} . Before the fallback time $T_{\text{fb}} = (1+z)t_{\text{fb}}$, we write down the isotropic equivalent energy of the jet

$$\int L_{\text{f,iso}} dt \sim \frac{4\pi}{3} R_{\text{f}}^2 \Gamma_{\text{f}}^3 n_{\text{ext}} m_p c^2.\tag{B8}$$

Noting $R_{\text{f}} \sim \Gamma_{\text{f}}^2 c T_{\text{obs}} / (1+z)$, we obtain the time dependence of Γ_{f} in the deceleration regime

$$\Gamma_{\text{f}} \propto T_{\text{obs}}^{-(2+\alpha)/8}, \text{ for } T_{\text{obs}} < T_{\text{fb}}.\tag{B9}$$

After T_{fb} , $L_{\text{f,iso}}$ decays faster than t^{-1} , which implies

$$\mathcal{E}_{\text{f,iso}} \sim \frac{4\pi}{3} R_{\text{f}}^3 \Gamma_{\text{f}}^2 n_{\text{ext}} m_p c^2 = \text{const},\tag{B10}$$

and

$$\Gamma_{\text{f}} \propto T_{\text{obs}}^{-3/8}, \text{ for } T_{\text{obs}} > T_{\text{fb}}.\tag{B11}$$

The analytical solutions are consistent with Fig. 2.

B.2. *Fast Jet Forward Shock*

Given the parameters in Table 1, the injected electrons are in the fast cooling regime, i.e., the electron minimum Lorentz factor $\gamma_{e,m}^{\text{fs}}$ is larger than the cooling Lorentz factor

$$\gamma_{e,c}^{\text{fs}} = \frac{6\pi m_e c}{(1+Y)\sigma_T B_{\text{fs}}^2 t'_{\text{dyn}}} \quad (\text{B12})$$

where $Y \sim \mathcal{O}(\sqrt{\epsilon_e/\epsilon_B})$ is the Compton parameter (Sari & Esin 2001), σ_T is the Thomson cross section, and $t'_{\text{dyn}} = R_f/(\Gamma_f c)$ is the comoving dynamic time. We estimate the peak synchrotron flux (e.g., Wijers & Galama 1999)

$$F_{\nu,\text{max}}^{(\text{fs})} = \frac{(1+z)f_{\text{br}}(0.6f_e^{\text{fs}}n_{\text{ext}}R_f^3)\Gamma_f e^3 B_{\text{fs}}}{\sqrt{3}m_e c^2 d_L^2} \sim 9.3 \times 10^{-27} \text{erg s}^{-1} \text{cm}^{-2} \text{Hz}^{-1} f_{\text{br}} n_{\text{ext},0.3}^{3/2} \Gamma_{f,0.8}^8 (T_{\text{obs}}/15 \text{d})^3. \quad (\text{B13})$$

In the X-ray bands, e.g., $E_X = 10 \text{keV} = h\nu_X$, we infer the energy flux

$$\nu F_{\nu}^{(\text{fs})} = F_{\nu,\text{max}}^{(\text{fs})} \nu_c^{1/2} \nu_m^{(s-1)/2} \nu_X^{(1-s/2)} \sim 8.1 \times 10^{-14} \text{erg s}^{-1} \text{cm}^{-2}, \quad (\text{B14})$$

where $\nu_c = 3\Gamma_f(\gamma_{e,c}^{\text{fs}})^2 eB/[4\pi(1+z)m_e c]$ is the cooling frequency. The analytical value is consistent with the gray dashed curves in Fig. 3. Meanwhile, we derive the time dependence of the X-ray emissions produced by forward shock

$$\nu F_{\nu}^{(\text{fs})}(E_X) \propto \begin{cases} f_{\text{br}} T_{\text{obs}}^{-\alpha+1-s/2}, & T_{\text{obs}} < T_{\text{br}} \simeq T_{\text{fb}} \\ f_{\text{br}} T_{\text{obs}}^{-1}, & T_{\text{obs}} > T_{\text{br}} \simeq T_{\text{fb}}, \end{cases} \quad (\text{B15})$$

where $f_{\text{br}} = 1/[1 + (\Gamma_f \theta_f)^{-2}]$ is the jet break factor. In our calculation, we infer the jet break time, defined via $\Gamma_f(t_{\text{br}}) = 1/\theta_f$, to be $t_{\text{br}} \simeq 2.8 \times 10^6 \text{s} \simeq t_{\text{fb}}$, which implies a steepened lightcurve for $T_{\text{obs}} > T_{\text{br}} \simeq T_{\text{fb}}$, $\nu F_{\nu}^{(\text{fs})}(E_X) \propto \Gamma_f^2 T_{\text{obs}}^{-1} \propto T_{\text{obs}}^{-7/4}$, noting that $\Gamma_f \propto T_{\text{obs}}^{-3/8}$. Eq. B15 indicates that the forward shock afterglow is disfavored to explain the fast decay of the X-ray lightcurve before and after the fallback time, since it predicts a subdominant slow decaying X-ray lightcurve.

B.3. *Fast Jet Reverse Shock*

In the deceleration regime, we have the relative Lorentz factor between the reverse shock up and downstreams $\Gamma_{f,\text{rs-rel}} = (\Gamma_{f0}/\Gamma_f + \Gamma_f/\Gamma_{f0})/2$. The electrons accelerated in the reverse shock region are fast cooling using the parameters in Table 1. Given the accelerated electron number in the reverse shock downstream, $N_{e,\text{rs}} \sim f_e^{\text{rs}} \Gamma_{f,\text{rs-rel}} n'_{f,\text{rs}} (4\pi R_f^2)(R_f/\Gamma_f)$, we write down the maximum synchrotron flux at $T_{\text{obs}} = 15 \text{d}$

$$F_{\nu,\text{max}}^{\text{rs}} = \frac{0.6 f_{\text{br}} \sqrt{3} (1+z) N_{e,\text{rs}} \Gamma_f e^3 B_{f,\text{rs}}}{4\pi m_e c^2 d_L^2} \simeq 1.2 \times 10^{-26} \text{erg s}^{-1} \text{cm}^{-2} \text{Hz}^{-1} \quad (\text{B16})$$

where fiducial values are used to calculate $L_{f,\text{iso}}$, $\Gamma_{f,\text{rs-rel}}$ and $B_{f,\text{rs}}$. From Fig. 3, we observe the relationship $\nu_X \gtrsim \nu_m > \nu_c$, where $\nu_m \propto \Gamma_f(\gamma_{e,m}^{\text{rs}})^2 B_{\text{rs}}$ is the characteristic frequency and ν_c is the cooling frequency defined similar to the forward shock case. In this case, we calculate the X-ray energy flux at $T_{\text{obs}} = 15 \text{d}$ using the cooling frequency of the reverse shock regime,

$$\nu F_{\nu}^{(\text{rs})}(E_X) = \nu_c^{1/2} \nu_m^{(s-1)/2} \nu_X^{(1-s/2)} F_{\nu,\text{max}}^{\text{rs}} \sim 1.7 \times 10^{-12} \text{erg s}^{-1} \text{cm}^{-2}. \quad (\text{B17})$$

We also check the time evolution of X-ray lightcurves

$$\nu F_{\nu}^{(\text{rs})}(E_X) \propto \nu_c^{1/2} \nu_m^{(s-1)/2} F_{\nu,\text{max}}^{\text{rs}} \propto \begin{cases} f_{\text{br}} T_{\text{obs}}^{-[5\alpha+\alpha(s-1)]/4}, & T_{\text{obs}} < T_{\text{br}} \simeq T_{\text{fb}} \\ f_{\text{br}} T_{\text{obs}}^{-(s+8)/6}, & T_{\text{obs}} > T_{\text{br}} \simeq T_{\text{fb}}. \end{cases} \quad (\text{B18})$$

Similar to the forward shock case, considering the jet break correction, we obtain a steepened lightcurve for $T_{\text{obs}} > T_{\text{fb}} \simeq T_{\text{br}}$, $\nu F_{\nu}^{(\text{rs})}(E_X) \propto \Gamma_f^2 T_{\text{obs}}^{-(s+8)/6} \propto T_{\text{obs}}^{-(2s+25)/12} \propto T_{\text{obs}}^{-2.5}$ for $s = 2.3$. Since we adopted the approximations, $\Gamma_{f,\text{rs-rel}} \sim \Gamma_{f,\text{rs-rel}} - 1 \sim \Gamma_{f0}/(2\Gamma_f)$, to obtain Eq. 20, the numerical time decay slope could be steeper by a correction factor $\sim T_{\text{obs}}^{-0.2} - T_{\text{obs}}^{-0.4}$. In this case, the analytical lightcurve aligns well with numerical results depicted in Fig. 4 and is in agreement with late-time X-ray upper limits (the red triangles in Fig. 4).

REFERENCES

- Andreoni, I., Coughlin, M. W., Perley, D. A., et al. 2022, *Nature*, 612, 430, doi: 10.1038/s41586-022-05465-8
- Barniol Duran, R., Nakar, E., & Piran, T. 2013, *ApJ*, 772, 78, doi: 10.1088/0004-637X/772/1/78

- Berger, E., Zauderer, A., Pooley, G. G., et al. 2012, *ApJ*, 748, 36, doi: [10.1088/0004-637X/748/1/36](https://doi.org/10.1088/0004-637X/748/1/36)
- Blandford, R. D., & McKee, C. F. 1976, *Physics of Fluids*, 19, 1130, doi: [10.1063/1.861619](https://doi.org/10.1063/1.861619)
- Bloom, J. S., Giannios, D., Metzger, B. D., et al. 2011, *Science*, 333, 203, doi: [10.1126/science.1207150](https://doi.org/10.1126/science.1207150)
- Brown, G. C., Levan, A. J., Stanway, E. R., et al. 2015, *MNRAS*, 452, 4297, doi: [10.1093/mnras/stv1520](https://doi.org/10.1093/mnras/stv1520)
- Burrows, D. N., Kennea, J. A., Ghisellini, G., et al. 2011, *Nature*, 476, 421, doi: [10.1038/nature10374](https://doi.org/10.1038/nature10374)
- Cendes, Y., Eftekhari, T., Berger, E., & Polinsky, E. 2021, *ApJ*, 908, 125, doi: [10.3847/1538-4357/abd323](https://doi.org/10.3847/1538-4357/abd323)
- Cenko, S. B., Krimm, H. A., Horesh, A., et al. 2012, *ApJ*, 753, 77, doi: [10.1088/0004-637X/753/1/77](https://doi.org/10.1088/0004-637X/753/1/77)
- Chevalier, R. A. 1998, *ApJ*, 499, 810, doi: [10.1086/305676](https://doi.org/10.1086/305676)
- Crumley, P., Lu, W., Santana, R., et al. 2016, *MNRAS*, 460, 396, doi: [10.1093/mnras/stw967](https://doi.org/10.1093/mnras/stw967)
- Dai, L., & Fang, K. 2017, *MNRAS*, 469, 1354, doi: [10.1093/mnras/stx863](https://doi.org/10.1093/mnras/stx863)
- Eftekhari, T., Berger, E., Zauderer, B. A., Margutti, R., & Alexander, K. D. 2018, *ApJ*, 854, 86, doi: [10.3847/1538-4357/aaa8e0](https://doi.org/10.3847/1538-4357/aaa8e0)
- Eftekhari, T., Tchekhovskoy, A., Alexander, K. D., et al. 2024, arXiv e-prints, arXiv:2404.10036, doi: [10.48550/arXiv.2404.10036](https://doi.org/10.48550/arXiv.2404.10036)
- Evans, C. R., & Kochanek, C. S. 1989, *ApJ*, 346, L13, doi: [10.1086/185567](https://doi.org/10.1086/185567)
- Giannios, D., & Metzger, B. D. 2011, *MNRAS*, 416, 2102, doi: [10.1111/j.1365-2966.2011.19188.x](https://doi.org/10.1111/j.1365-2966.2011.19188.x)
- Hayasaki, K. 2021, *Nature Astronomy*, 5, 436, doi: [10.1038/s41550-021-01309-z](https://doi.org/10.1038/s41550-021-01309-z)
- Hills, J. G. 1975, *Nature*, 254, 295, doi: [10.1038/254295a0](https://doi.org/10.1038/254295a0)
- Huang, Y. F., Dai, Z. G., & Lu, T. 1999, *MNRAS*, 309, 513, doi: [10.1046/j.1365-8711.1999.02887.x](https://doi.org/10.1046/j.1365-8711.1999.02887.x)
- Ioka, K., Kobayashi, S., & Zhang, B. 2005, *ApJ*, 631, 429, doi: [10.1086/432567](https://doi.org/10.1086/432567)
- Jiang, N., Zhou, Z., Zhu, J., Wang, Y., & Wang, T. 2023, *ApJ*, 953, L12, doi: [10.3847/2041-8213/acebe3](https://doi.org/10.3847/2041-8213/acebe3)
- Kippenhahn, R., & Weigert, A. 1990, *Stellar Structure and Evolution*
- Klinger, M., Rudolph, A., Rodrigues, X., et al. 2023, arXiv e-prints, arXiv:2312.13371, doi: [10.48550/arXiv.2312.13371](https://doi.org/10.48550/arXiv.2312.13371)
- Liu, D., Pe'er, A., & Loeb, A. 2015, *ApJ*, 798, 13, doi: [10.1088/0004-637X/798/1/13](https://doi.org/10.1088/0004-637X/798/1/13)
- Liu, R.-Y., Xi, S.-Q., & Wang, X.-Y. 2020, *Phys. Rev. D*, 102, 083028, doi: [10.1103/PhysRevD.102.083028](https://doi.org/10.1103/PhysRevD.102.083028)
- Lunardini, C., & Winter, W. 2017, *Phys. Rev. D*, 95, 123001, doi: [10.1103/PhysRevD.95.123001](https://doi.org/10.1103/PhysRevD.95.123001)
- Matsumoto, T., & Metzger, B. D. 2023, *MNRAS*, 522, 4028, doi: [10.1093/mnras/stad1182](https://doi.org/10.1093/mnras/stad1182)
- Metzger, B. D., Giannios, D., & Mimica, P. 2012, *MNRAS*, 420, 3528, doi: [10.1111/j.1365-2966.2011.20273.x](https://doi.org/10.1111/j.1365-2966.2011.20273.x)
- Mimica, P., Giannios, D., Metzger, B. D., & Aloy, M. A. 2015, *MNRAS*, 450, 2824, doi: [10.1093/mnras/stv825](https://doi.org/10.1093/mnras/stv825)
- Mukhopadhyay, M., Bhattacharya, M., & Murase, K. 2023, arXiv e-prints, arXiv:2309.02275, doi: [10.48550/arXiv.2309.02275](https://doi.org/10.48550/arXiv.2309.02275)
- Murase, K., Kimura, S. S., Zhang, B. T., Oikonomou, F., & Petropoulou, M. 2020, *ApJ*, 902, 108, doi: [10.3847/1538-4357/abb3c0](https://doi.org/10.3847/1538-4357/abb3c0)
- Murase, K., Mészáros, P., & Fox, D. B. 2017, *ApJ*, 836, L6, doi: [10.3847/2041-8213/836/1/L6](https://doi.org/10.3847/2041-8213/836/1/L6)
- Nava, L., Sironi, L., Ghisellini, G., Celotti, A., & Ghirlanda, G. 2013, *MNRAS*, 433, 2107, doi: [10.1093/mnras/stt872](https://doi.org/10.1093/mnras/stt872)
- Pasham, D. R., Lucchini, M., Laskar, T., et al. 2023, *Nature Astronomy*, 7, 88, doi: [10.1038/s41550-022-01820-x](https://doi.org/10.1038/s41550-022-01820-x)
- Pe'er, A. 2012, *ApJ*, 752, L8, doi: [10.1088/2041-8205/752/1/L8](https://doi.org/10.1088/2041-8205/752/1/L8)
- Phinney, E. S. 1989, in *The Center of the Galaxy*, ed. M. Morris, Vol. 136, 543
- Piran, T., Svirski, G., Krolik, J., Cheng, R. M., & Shiokawa, H. 2015, *ApJ*, 806, 164, doi: [10.1088/0004-637X/806/2/164](https://doi.org/10.1088/0004-637X/806/2/164)
- Rees, M. J. 1988, *Nature*, 333, 523, doi: [10.1038/333523a0](https://doi.org/10.1038/333523a0)
- Reis, R. C., Miller, J. M., Reynolds, M. T., et al. 2012, *Science*, 337, 949, doi: [10.1126/science.1223940](https://doi.org/10.1126/science.1223940)
- Reusch, S., Stein, R., Kowalski, M., et al. 2022, *Phys. Rev. Lett.*, 128, 221101, doi: [10.1103/PhysRevLett.128.221101](https://doi.org/10.1103/PhysRevLett.128.221101)
- Rhodes, L., Bright, J. S., Fender, R., et al. 2023, *MNRAS*, 521, 389, doi: [10.1093/mnras/stad344](https://doi.org/10.1093/mnras/stad344)
- Rossi, E., Lazzati, D., & Rees, M. J. 2002, *MNRAS*, 332, 945, doi: [10.1046/j.1365-8711.2002.05363.x](https://doi.org/10.1046/j.1365-8711.2002.05363.x)
- Sari, R., & Esin, A. A. 2001, *ApJ*, 548, 787, doi: [10.1086/319003](https://doi.org/10.1086/319003)
- Sato, Y., Murase, K., Bhattacharya, M., et al. 2024, arXiv e-prints, arXiv:2404.13326, doi: [10.48550/arXiv.2404.13326](https://doi.org/10.48550/arXiv.2404.13326)
- Sato, Y., Obayashi, K., Yamazaki, R., Murase, K., & Ohira, Y. 2021, *MNRAS*, 504, 5647, doi: [10.1093/mnras/stab1273](https://doi.org/10.1093/mnras/stab1273)
- Senno, N., Murase, K., & Mészáros, P. 2017, *ApJ*, 838, 3, doi: [10.3847/1538-4357/aa6344](https://doi.org/10.3847/1538-4357/aa6344)
- Shen, R.-F., & Matzner, C. D. 2014, *ApJ*, 784, 87, doi: [10.1088/0004-637X/784/2/87](https://doi.org/10.1088/0004-637X/784/2/87)
- Stein, R., van Velzen, S., Kowalski, M., et al. 2021, *Nature Astronomy*, 5, 510, doi: [10.1038/s41550-020-01295-8](https://doi.org/10.1038/s41550-020-01295-8)

- Teboul, O., & Metzger, B. D. 2023, *ApJ*, 957, L9,
doi: [10.3847/2041-8213/ad0037](https://doi.org/10.3847/2041-8213/ad0037)
- van Velzen, S., Stein, R., Gilfanov, M., et al. 2021, arXiv e-prints, arXiv:2111.09391,
doi: [10.48550/arXiv.2111.09391](https://doi.org/10.48550/arXiv.2111.09391)
- Wang, J.-Z., Lei, W.-H., Wang, D.-X., et al. 2014, *ApJ*, 788, 32, doi: [10.1088/0004-637X/788/1/32](https://doi.org/10.1088/0004-637X/788/1/32)
- Wang, X.-Y., & Liu, R.-Y. 2016, *Phys. Rev. D*, 93, 083005,
doi: [10.1103/PhysRevD.93.083005](https://doi.org/10.1103/PhysRevD.93.083005)
- Wijers, R. A. M. J., & Galama, T. J. 1999, *ApJ*, 523, 177,
doi: [10.1086/307705](https://doi.org/10.1086/307705)
- Winter, W., & Lunardini, C. 2021, *Nature Astronomy*, 5, 472, doi: [10.1038/s41550-021-01305-3](https://doi.org/10.1038/s41550-021-01305-3)
- . 2023, *ApJ*, 948, 42, doi: [10.3847/1538-4357/acbe9e](https://doi.org/10.3847/1538-4357/acbe9e)
- Yao, Y., Lu, W., Harrison, F., et al. 2024, *ApJ*, 965, 39,
doi: [10.3847/1538-4357/ad2b6b](https://doi.org/10.3847/1538-4357/ad2b6b)
- Yuan, C., Murase, K., Kimura, S. S., & Mészáros, P. 2020, *Phys. Rev. D*, 102, 083013,
doi: [10.1103/PhysRevD.102.083013](https://doi.org/10.1103/PhysRevD.102.083013)
- Yuan, C., Murase, K., Zhang, B. T., Kimura, S. S., & Mészáros, P. 2021, *ApJ*, 911, L15,
doi: [10.3847/2041-8213/abee24](https://doi.org/10.3847/2041-8213/abee24)
- Yuan, C., & Winter, W. 2023, *ApJ*, 956, 30,
doi: [10.3847/1538-4357/acf615](https://doi.org/10.3847/1538-4357/acf615)
- Yuan, C., Winter, W., & Lunardini, C. 2024, arXiv e-prints, arXiv:2401.09320, doi: [10.48550/arXiv.2401.09320](https://doi.org/10.48550/arXiv.2401.09320)
- Zauderer, B. A., Berger, E., Margutti, R., et al. 2013, *ApJ*, 767, 152, doi: [10.1088/0004-637X/767/2/152](https://doi.org/10.1088/0004-637X/767/2/152)
- Zauderer, B. A., Berger, E., Soderberg, A. M., et al. 2011, *Nature*, 476, 425, doi: [10.1038/nature10366](https://doi.org/10.1038/nature10366)
- Zhang, B. 2018, *The physics of gamma-ray bursts* (Cambridge University Press)
- Zhang, B., & Mészáros, P. 2002, *ApJ*, 571, 876,
doi: [10.1086/339981](https://doi.org/10.1086/339981)
- Zhang, B. T., Murase, K., Ioka, K., & Zhang, B. 2023, arXiv e-prints, arXiv:2311.13671,
doi: [10.48550/arXiv.2311.13671](https://doi.org/10.48550/arXiv.2311.13671)
- Zhang, B. T., Murase, K., Veres, P., & Mészáros, P. 2021, *ApJ*, 920, 55, doi: [10.3847/1538-4357/ac0cfc](https://doi.org/10.3847/1538-4357/ac0cfc)
- Zhou, C., Zhu, Z.-P., Lei, W.-H., et al. 2024, *ApJ*, 963, 66,
doi: [10.3847/1538-4357/ad20f3](https://doi.org/10.3847/1538-4357/ad20f3)